Hindawi Publishing Corporation
Mathematical Problems in Engineering
Volume 2015, Article ID 327347, 9 pages
http://dx.doi.org/10.1155/2015/327347

Research Article

Research on Adaptive Dual-Mode Switch Control Strategy for Vehicle Maglev Flywheel Battery

Hui Gao, Ying-Jun Wu, and Jing-Jin Shen

Nanjing University of Posts and Telecommunications, Nanjing 210023, China

Correspondence should be addressed to Hui Gao; gaohui2005@163.com

Received 3 November 2014; Accepted 15 January 2015

Academic Editor: Honglei Xu

Because of the jamming signal is real-time changeable and control algorithm cannot timely tracking control flywheel rotor, this paper takes vehicle maglev flywheel battery as the research object. One kind of dual-model control strategy is developed based on the analysis of the vibration response impact of the flywheel battery control system. In view of the complex foundation vibration problems of electric vehicles, the nonlinear dynamic simulation model of vehicle maglev flywheel battery is solved. Through analyzing the nonlinear vibration response characteristics, one kind of dual-mode adaptive hybrid control strategy based on $H\infty$ control and unbalance displacement feed-forward compensation control is presented and a real-time switch controller is designed. The reliable hybrid control is implemented, and the stability in the process of real-time switch is solved. The results of this project can provide important basic theory support for the research of vehicle maglev flywheel battery control system.

1. Introduction

As the future main traffic tools, electric vehicle (EV) is required in the performance of starting, acceleration, and climbing; however, this performance depends largely on the power battery performance [1]. But, the faults of costly, short range and short service life become the bottleneck to restrict EV development scale. Specifically in the process of frequent start-stop or climbing, the chemical battery life is more shorten because of fast and deep discharging [2, 3]. How to eliminate these shortcomings becomes the key EV to be quickly developed.

Maglev flywheel can be applied in EV electric power system, aerospace, and other fields because of having high specific energy, high power, fast charge and discharge, long service life, no waste gas pollution, environment-friendly advantages, and so on [4–6]. In the field of EV, the maglev flywheel either can be as an independent power driving EV [3], or can be used as auxiliary power assisting the motive power batteries work [7, 8]. However, the maglev flywheel control stability will be affected because of existing start-stop, acceleration and deceleration, steering, and road random vibration in the process of the EV driving and even cause instability. So, the efficiency of magnetic suspension flywheel must be reduced.

For the scientific research and practical application of maglev flywheel, a dual-mode adaptive hybrid control strategy is studied based on $H\infty$ control and AILC algorithms, and the state space equation of maglev flywheel was analyzed. To improve the robust stability of flywheel control system and reduce the real-time interference, one $H\infty$ controller based on the state space equation was solved. To reduce maglev flywheel radial run-out, one adaptive iterative learning control theory was deduced and unbalance displacement compensation was implemented. The experimental result shows the dual-model control strategy has better interference capability in maglev flywheel start-up process and has stronger active control ability relative to only PID control. The maglev flywheel based on the dual-model control can help the EV primary battery, improve its discharge characteristics, and help to prolong its service life.

2. Maglev Flywheel Nonlinear Dynamic Model

The below force and movement differential equation of the flywheel are discussed in order to solve the maglev flywheel nonlinear dynamic model. Figure 1 shows the below force of the flywheel.

In Figure 1, O-XYZ is the space coordinate, 1 and 2 are, respectively, the left and right position of the radial magnetic

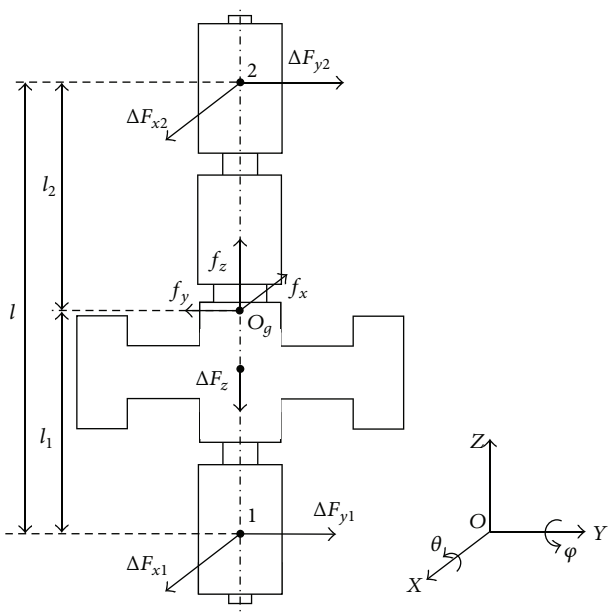

Figure 1: Flywheel below force analysis.

bearing, $O_g\,(x_g, y_g, z_g)$ is the mass center of the flywheel, l is the distance between 1 and 2, l_1 is the distance from the mass center to 1, l_2 is the distance from the mass center to 2, φ and θ are, respectively, the angular displacements around the x-axis and y-axis, ΔF_{x1}, ΔF_{x2}, ΔF_{y1}, ΔF_{y2}, and ΔF_z are the electromagnetic force of the flywheel in the three axes, and f_x, f_y, and f_z are the disturbing force and the unbalance force of the flywheel in the three axes. The flywheel movement differential equations are deduced according to the below force analysis in Figure 1 and the motion laws of particles [9]:

$$\begin{aligned} m\ddot{x}_g &= \Delta F_{x1} + \Delta F_{x2} - f_x, \\ m\ddot{y}_g &= \Delta F_{y1} + \Delta F_{y2} - f_y, \\ I_r\ddot{\varphi} - \omega I_a\dot{\theta} &= \Delta F_{y1}\cdot l_1 - \Delta F_{y2}\cdot l_2, \\ I_r\ddot{\theta} + \omega I_a\dot{\varphi} &= -\Delta F_{x1}\cdot l_1 + \Delta F_{x2}\cdot l_2, \\ m\ddot{z}_g &= \Delta F_z - f_z, \end{aligned} \tag{1}$$

where m is the flywheel quality, I_r and I_a are, respectively, the radial inertia moment and axial inertia moment, and ω is the angular velocity of the flywheel. The motion differential equation of matrix form can be written by [10]

$$\begin{aligned} &\begin{pmatrix} \frac{l_2}{l}m & \frac{l_1}{l}m & 0 & 0 & 0 \\ 0 & 0 & \frac{l_2}{l}m & \frac{l_1}{l}m & 0 \\ 0 & 0 & -\frac{I_r}{l} & \frac{I_r}{l} & 0 \\ -\frac{I_r}{l} & \frac{I_r}{l} & 0 & 0 & 0 \\ 0 & 0 & 0 & 0 & m \end{pmatrix} \begin{pmatrix} \ddot{x}_1 \\ \ddot{x}_2 \\ \ddot{y}_1 \\ \ddot{y}_2 \\ \ddot{z} \end{pmatrix} \\ &+ \begin{pmatrix} 0 & 0 & 0 & 0 & 0 \\ 0 & 0 & 0 & 0 & 0 \\ \frac{\omega I_a}{l} & -\frac{\omega I_a}{l} & 0 & 0 & 0 \\ 0 & 0 & -\frac{\omega I_a}{l} & \frac{\omega I_a}{l} & 0 \\ 0 & 0 & 0 & 0 & 0 \end{pmatrix} \begin{pmatrix} \dot{x}_1 \\ \dot{x}_2 \\ \dot{y}_1 \\ \dot{y}_2 \\ \dot{z} \end{pmatrix} \\ &= \begin{pmatrix} k_{xx1} & k_{xx2} & 0 & 0 & 0 \\ 0 & 0 & k_{xy1} & k_{xy2} & 0 \\ 0 & 0 & l_1k_{xy1} & -l_2k_{xy2} & 0 \\ -l_1k_{xx1} & l_2k_{xx2} & 0 & 0 & 0 \\ 0 & 0 & 0 & 0 & k_{xz} \end{pmatrix} \begin{pmatrix} x_1 \\ x_2 \\ y_1 \\ y_2 \\ z \end{pmatrix} \\ &+ \begin{pmatrix} k_{ix1} & k_{ix2} & 0 & 0 & 0 \\ 0 & 0 & k_{iy1} & k_{iy2} & 0 \\ 0 & 0 & l_1k_{iy1} & -l_2k_{iy2} & 0 \\ -l_1k_{ix1} & l_2k_{ix2} & 0 & 0 & 0 \\ 0 & 0 & 0 & 0 & k_{iz} \end{pmatrix} \begin{pmatrix} i_{cx1} \\ i_{cx2} \\ i_{cy1} \\ i_{cy2} \\ i_{cz} \end{pmatrix} \\ &+ \begin{pmatrix} 1 & 0 & 0 & 0 & 0 \\ 0 & 1 & 0 & 0 & 0 \\ 0 & 0 & 1 & 0 & 0 \\ 0 & 0 & 0 & 1 & 0 \\ 0 & 0 & 0 & 0 & 1 \end{pmatrix} \begin{pmatrix} f_x \\ f_y \\ 0 \\ 0 \\ f_z \end{pmatrix}, \end{aligned} \tag{2}$$

where x_1, x_2, y_1, y_2, and z are the displacements of the flywheel in five freedom degrees, i_{cx1}, i_{cx2}, i_{cy1}, i_{cy1}, and i_{cz} are, respectively, the control current corresponding to each freedom degree, k_{xx1}, k_{xx2}, k_{xy1}, k_{xy2}, and k_{xz} are, respectively, the displacement stiffness of each freedom degree, and k_{ix1}, k_{ix2}, k_{iy1}, k_{iy2}, and k_{iz} are, respectively, the current stiffness of each freedom degree.

For the convenience of analysis, type (2) can be expressed by type (3):

$$\mathbf{M}\ddot{\mathbf{x}} + \mathbf{C}\dot{\mathbf{x}} + \mathbf{K}\mathbf{x} = \mathbf{B}\mathbf{i_c} + \mathbf{I}\mathbf{f}, \tag{3}$$

where $\mathbf{M}$ is the mass matrix, $\mathbf{C}$ is the damping coefficient matrix, $\mathbf{K}$ is the displacement stiffness matrix, $\mathbf{B}$ is the current stiffness matrix, $\mathbf{I}$ is the unit matrix, $\mathbf{x}$ is the displacement vector, $\mathbf{i_c}$ is the control current vector, and $\mathbf{f}$ is the unbalanced inertial force vector. Type (3) can be rewritten as

$$\ddot{\mathbf{x}} = -\frac{\mathbf{C}}{\mathbf{M}}\dot{\mathbf{x}} - \frac{\mathbf{K}}{\mathbf{M}}\mathbf{x} + \frac{\mathbf{B}}{\mathbf{M}}\mathbf{i_c} + \frac{\mathbf{I}}{\mathbf{M}}\mathbf{f}. \tag{4}$$

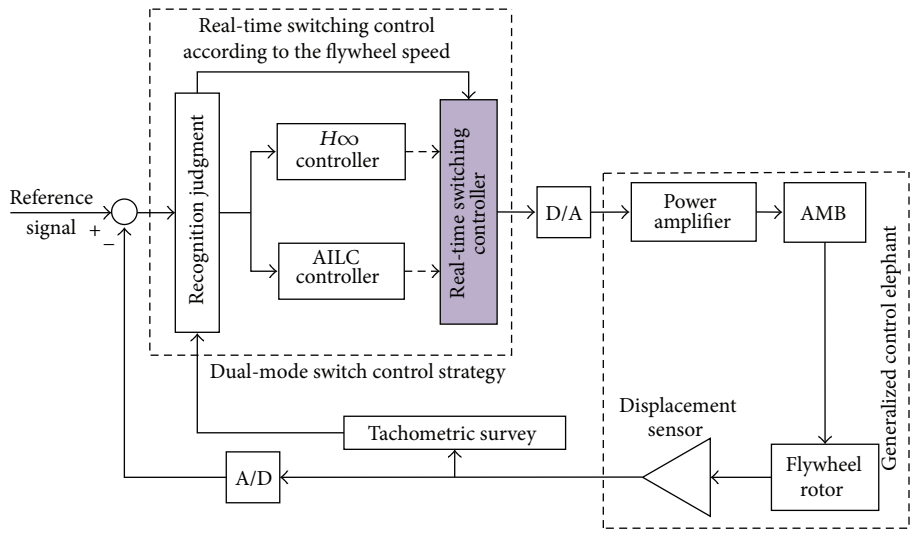

Figure 2: The dual-mode switch control strategy diagram.

The state space of the flywheel system transfer function matrix $G(s)$ is

$$\begin{aligned} \bar{\mathbf{x}} &= \mathbf{A}\bar{\mathbf{x}} + \mathbf{B}_1\mathbf{f} + \mathbf{B}_2\mathbf{u}, \\ \mathbf{y} &= \mathbf{C}\bar{\mathbf{x}}, \end{aligned} \tag{5}$$

where $\bar{\mathbf{x}} = [\mathbf{x}\ \ \dot{\mathbf{x}}]^{\mathbf{T}}$ is the state vector, $\mathbf{u} = \mathbf{i_c}$ is the vector control, $\mathbf{y} = \mathbf{x}$ is the measured quantity, namely, the sensor output signal vector of the five freedom degrees. Moreover, type (5) can also be expressed as

$$\mathbf{G}(s) = \begin{bmatrix} G_{11}(s) & G_{12}(s) \\ G_{21}(s) & G_{22}(s) \end{bmatrix} = \left[\begin{array}{c|cc} \mathbf{A} & \mathbf{B}_1 & \mathbf{B}_2 \\ \hline \mathbf{C} & O & O \end{array}\right], \tag{6}$$

where O is the five-order zero matrix; it can be solved out through types (4) and (5):

$$\begin{aligned} \mathbf{A} &= \begin{bmatrix} O & \mathbf{I} \\ -\dfrac{\mathbf{K}}{\mathbf{M}} & -\dfrac{\mathbf{C}}{\mathbf{M}} \end{bmatrix}, \qquad \mathbf{B}_1 = \begin{bmatrix} O \\ \dfrac{\mathbf{I}}{\mathbf{M}} \end{bmatrix}, \\ \mathbf{B}_2 &= \begin{bmatrix} O \\ -\dfrac{\mathbf{I}}{\mathbf{M}} \end{bmatrix}, \qquad \mathbf{C} = [\mathbf{I}\ \ O]. \end{aligned} \tag{7}$$

So far, the nonlinear dynamic model $G(s)$ of the maglev flywheel is solved, and the precise model is provided for the design of the following dual-mode switch controller.

3. Dual-Mode Switch Control Strategy

To improve the control stability and the energy storage density of vehicle maglev flywheel, a dual-mode switch control strategy is study based on $H\infty$ control algorithm and adaptive iterative learning control algorithm. The control strategy is shown in Figure 2. The control strategy includes generalized control elephant and dual-mode switch controller. Among them, the generalized control elephant is composed of power amplifiers, active magnetic bearing (AMB), flywheel rotor, and displacement and the dual-mode switch controller is composed of $H\infty$ controller and unbalance compensation controller.

The basic response is a random signal when EV is driving on the bumpy road or start-stop, acceleration-deceleration, and steering. To reduce the random impact and improve the control robustness, a $H\infty$ controller is solved. Besides, to limit the flywheel radial run-out of the maglev flywheel battery in the charging process and improve the energy storage density of the maglev flywheel, an unbalance displacement feed-forward compensation controller based on adaptive iterative learning control (AILC) algorithm is adopted [10]. The switching work between $H\infty$ control and AILC is implemented by the real-time switching controller by judging the status of the EV and the maglev flywheel.

3.1. $H\infty$ Controller Design. A kind of $H\infty$ control strategy with mixed sensitivity is designed according to the characteristic of the maglev flywheel state space equation; it is shown in Figure 3.

In Figure 3, $\mathbf{K_H}$ is the transfer function matrix of the $H\infty$ controller, $\mathbf{u}$ is the input signal matrix, W_1, W_2, and W_3 are the weighted functions, $\mathbf{G}$ is the state space equation of the maglev flywheel (it contains the power amplifier transfer function G_A, the sensor transfer function G_S, and the control current $\mathbf{i_c}$, and so forth), $\mathbf{y}$ is the sensor output signal vector, $\mathbf{r}$ is the system reference signal vector, and $\mathbf{e}$ is the error signal matrix.

$\mathbf{T_c}$ is the closed transfer function in Figure 3 can be written as [11]

$$\mathbf{T_c} = F_l(\mathbf{G}, \mathbf{K}_H) = \mathbf{G}_{11} + \mathbf{G}_{12}\mathbf{K}_H(\mathbf{I} - \mathbf{G}_{22}\mathbf{K}_H)^{-1}\mathbf{G}_{21}, \tag{8}$$

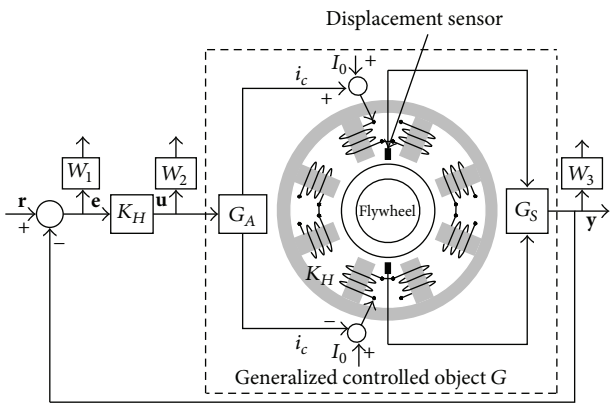

Figure 3: The diagram of $H\infty$ control strategy.

where type (8) is the linear fractional transformation of the $H\infty$ controller $\mathbf{K}_H$. The standard of $H\infty$ control problem is to find a real rational $\mathbf{K}_H$, to make the controlled object $\mathbf{G}$ stable work, and to make the minimal $H\infty$ norm of $\mathbf{T_c}$ in the whole frequency range [12], should be satisfied by

$$\|\mathbf{T_c}\|_\infty = \sup_\omega \overline{\sigma}\left(\mathbf{T_c}\left(j\omega\right)\right) < \gamma, \tag{9}$$

where $\overline{\sigma}(\mathbf{T_c}(j\omega))$ is the biggest singular value of $\mathbf{T_c}$, "sup" is the supremum of $\overline{\sigma}(\mathbf{T_c}(j\omega))$ in the whole frequency range, and γ is a given positive number.

The corresponding sensitivity and complementary sensitivity matrix functions $\mathbf{S}$ and $\mathbf{T}$ combined with Figure 2 can be deduced:

$$\begin{aligned} \mathbf{S} &= \frac{\mathbf{e}}{\mathbf{r}} = \frac{1}{\mathbf{I} + \mathbf{K}_H(s)\,\mathbf{G}(s)}, \\ \mathbf{T} &= \frac{\mathbf{y}}{\mathbf{r}} = \frac{\mathbf{K}_H(s)\,\mathbf{G}(s)}{\mathbf{I} + \mathbf{K}_H(s)\,\mathbf{G}(s)} = \mathbf{I} - \mathbf{S}. \end{aligned} \tag{10}$$

$W_1(s)$ is the weighted function of $\mathbf{S}$; its main purpose is to limit the amplitude of $\mathbf{S}$ in a specified frequency range. $W_3(s)$ is the weighted function of $\mathbf{T}$, whose purpose is to limit the amplitude of $\mathbf{T}$. In addition, the transfer function matrix of the $H\infty$ controller output is

$$\mathbf{R} = \frac{\mathbf{u}}{\mathbf{r}} = \frac{\mathbf{K}_H(s)}{\mathbf{I} + \mathbf{K}_H(s)\,\mathbf{G}(s)}. \tag{11}$$

$\mathbf{R}$ also has a weighted function $W_2(s)$; its main purpose is to limit the $\mathbf{K}_H$ controller output. $W_2(s)$ should be chosen as a relatively small value in order to reduce the compensators and shorten operation cycle.

The structural parameters of the maglev flywheel are calculated and got as $m = 10.8$ kg, $k_{ix1} = k_{ix2} = k_{iy1} = k_{iy2} = 954.6$ N/A, $k_{iz} = 1543.8$ N/A, $k_{xx1} = k_{xx2} = k_{xy1} = k_{xy2} = 1.517 \times 10^6$ N/m, and $K_{XZ} = 3.216 \times 10^6$ N/m. Based on $H\infty$ controller problem solving limit and MATLAB robust control instructions, the solved parameters are involved in the $\mathbf{G}(s)$ solution procedure, and the weighting functions $W_1(s)$ and $W_3(s)$ are determined, respectively, by

$$\begin{aligned} W_1(s) &= \frac{98}{s+2}, \\ W_3(s) &= \frac{1.5s}{s+3200}. \end{aligned} \tag{12}$$

In addition, $W_2(s)$ is selected as 2.0×10^7 through the simulation analysis. Then, the robust performance index (0.4232) is calculated based on the controlled object transfer function matrix $\mathbf{G}$ and the three weighted functions; if the index greater than 1, the three weighted functions need to be selected. Finally, the four radial and one axial discrete transfer functions of the $H\infty$ controller are concluded:

$$\begin{aligned} K_{Hx1} &= K_{Hx2} = K_{Hy1} = K_{Hy2} \\ &= \frac{-21.8z^3 + 15.3z^2 - 25.6z + 21.32}{z^3 - 10.61z^2 + 8.69z - 1.73}, \\ K_{Hz} &= \frac{-101.3z^3 + 80.5z^2 + 4.68}{z^3 - 5.87z^2 + 2.32z - 0.21}. \end{aligned} \tag{13}$$

Because the maglev flywheel is axially symmetric distribution in four radial freedom degrees, the four radial discrete transfer functions are the same. In order to make the control cycle consistent with the actual flywheel control system, the simulation sampling frequency is selected as 20000 Hz.

3.2. Feed-Forward Compensation Control Analysis. To reduce the radial run-out of the flywheel and solve the problem of variable speed, the AILC algorithm is adopted as the feed-forward controller to implement vibratory displacement compensation [10]. In Figure 4, the control scheme consists of PID feedback control system, AILC feed-forward compensation controller, and generalized plant. The PID controller can steady the whole system and improve the anti-interference ability, and the action of AILC is to make the learning gain accurately track the expectant orbit. The generalized plant includes power amplifier, electromagnetic coils, and rotor system.

To improve control performance and enhance the convergence rate of the learning law, there are two modifications in AILC. The first one is enhancing the error information action of previous control period and the second one is proposing a novel impacting factor β as the coefficient of the learning gain v_k. β can reduce the effects of learning gain to the control system when rotor speed does not coincide with the learning cycle of AILC. AILC can implement vibratory displacement compensation without any information of the generalized plant, and it will not increase the interference of the feedback controller. Only the expectant signal y_d and the output of the sensor y_k are needed in AILC; here, y_d is 2.5 V witch is defined as the balance position of rotor during static suspension. The error signal between y_d and y_k is iteratively learned, then, the perfect and unknown control signal u_k is obtained as the input signal of the power amplifier.

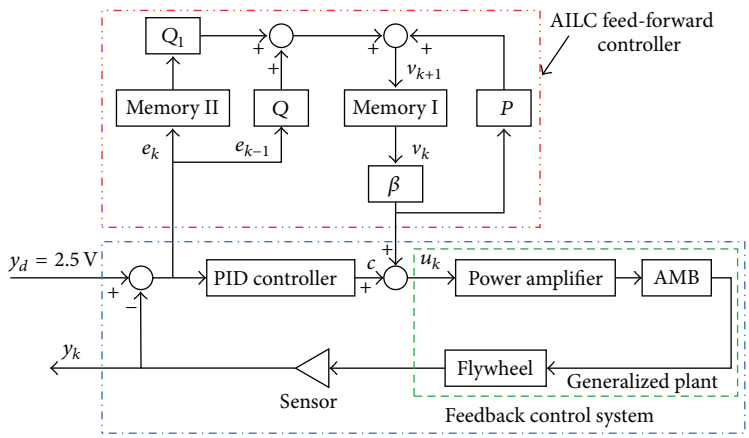

Figure 4: AILC compensation principle of AMB system.

The functions of AILC can be introduced by the iterative formulas in discrete domain. The error formula is given.

The update learning law of AILC is summarized as

$$v_{k+1}(n) = \beta P v_k(n) + Q e_k(n) + Q_1 e_k(n-1). \tag{14}$$

To understand the action of AILC better, the control input signal of generalized plant is written as

$$u_k(n) = c(n) + \beta v_k(n), \tag{15}$$

where $u_k(n)$ is the controller input, $c(n)$ is PID controller output, $v_k(n)$ is the learning gain of AILC, and β is the impacting factor of $v_k(n)$. The last objective is to obtain perfect controller signal u_d when having infinitely iterative learning and then make the error signal become zero. It should be satisfied as [13]

$$\lim_{k\to\infty} u_k(n) = u_d, \qquad \lim_{k\to\infty} e_k(n) = 0. \tag{16}$$

The discrete transfer function of the learning law of (14) can be calculated by

$$\begin{aligned} V_{k+1}(z) &= \beta P V_k(z) + Q E_k(z) + Q_1 E_k(z) z^{-1} \\ &= \beta P V_k(z) + \left(Q + Q_1 z^{-1}\right) E_k(z), \end{aligned} \tag{17}$$

where z^{-1} represents the lag operator in time domain, and it could make the sampled signal lag one period. This is the reason why the former error information is added into the modified learning law of AILC.

The PID controller with incomplete differential part is given in time domain:

$$\begin{aligned} c(t) &= G_P(t) \\ &= K_p\left[e(t) + \frac{1}{T_i}\int_0^t e(t)\,dt + \frac{T_d}{1+T_f}\frac{d(e(t))}{dt}\right]. \end{aligned} \tag{18}$$

The discrete function of (18) is deduced as

$$\begin{aligned} &C(z) \\ &= K_p\left[1 + \frac{T_0}{T_i}\frac{1}{1-z^{-1}} + \frac{T_d}{\left(1+T_f\right)T_0}\left(1-z^{-1}\right)\right]E(z). \end{aligned} \tag{19}$$

The z-transform of the control signal function of (15) is deduced by

$$\begin{aligned} U_k(z) &= C(z) + \beta V_k(z) \\ &= k_p\left[1 + \frac{T_0}{T_i}\frac{1}{1-z^{-1}} + \frac{T_d}{\left(1+T_f\right)T_0}\left(1-z^{-1}\right)\right]E(z) \\ &\quad + \beta V_k(z), \end{aligned} \tag{20}$$

where defining

$$\begin{aligned} &H(z) \\ &= 1\left(k_p\left[1 + \frac{T_0}{T_i}\frac{1}{1-z^{-1}} + \frac{T_d}{\left(1+T_f\right)T_0}\left(1-z^{-1}\right)\right]\right)^{-1}. \end{aligned} \tag{21}$$

The discrete function of error signal can be obtained as

$$E(z) = \left(U_k(z) - \beta V_k(z)\right)H(z). \tag{22}$$

Putting (22) into (17), it has

$$\begin{aligned} V_{k+1}(z) &= \beta P V_k(z) + \left(Q + Q_1 z^{-1}\right)\left(U_k(z) - \beta V_k(z)\right)H(z) \\ &= \beta\left[P - \left(Q + Q_1 z^{-1}\right)H(z)\right]V_k(z) \\ &\quad + \left(Q + Q_1 z^{-1}\right)H(z)U_k(z). \end{aligned} \tag{23}$$

Equation (24) gives the transformation in limit calculation at the two sides of (23)

$$V_\infty(z) = \lim_{k\to\infty} V_k(z) = \lim_{k\to\infty} \frac{\left(Q + Q_1 z^{-1}\right) H(z) U_k(z)}{1 - \beta\left[P + \left(Q + Q_1 z^{-1}\right) H(z)\right]}. \tag{24}$$

If P and β all are 1, at the same time, the following inequality is satisfied by [14]:

$$\left\| \beta P - \beta[Q + Q_1 z^{-1}] H(z) \right\|_\infty < 1. \tag{25}$$

Equation (24) can be simplified by

$$V_\infty(z) = \lim_{k\to\infty} U_k(z) = U_d(z). \tag{26}$$

That is, the controller signal $u_k(z)$ is replaced by $\beta v_k(z)$ when infinite iteration is operated, and the error signal will become zero. According to (22) and (26), the error signal can be shown as

$$\begin{aligned} \lim_{k\to\infty} E(z) &= H(z)\left[\lim_{k\to\infty} U_k(z) - \beta \lim_{k\to\infty} V_k(z)\right] \\ &= H(z)\left[U_d(z) - \beta V_\infty(z)\right] \\ &= H(z)\left[U_d(z) - \beta U_d(z)\right] = 0. \end{aligned} \tag{27}$$

The convergence of AILC has been demonstrated according to (26) and (27), and a perfect controller signal u_d has been obtained as power amplifier input. Therefore, the AILC algorithm as the feed-forward compensation controller can be adopted in the application of maglev flywheel unbalance vibratory compensation.

According to the start-up time and the variability of the rotor frequency from static suspension to one fixed speed, the equation of β is given as

$$\beta = \left(\frac{f}{f_d}\right)^n, \tag{28}$$

where f is the flywheel frequency, f_d is a given frequency, and the action of n is to reduce the value of β when f is far away from f_d (usually, n is greater than 2). In the start-up process, due to $f \ll f_d$, the value of β should be very small; it can weaken the influence of V_k on the generalized plant. However, β will be close to 1 if $f \approx f_d$; it can enhance the effect of repetitive learning and can make the error signal to converge toward zero.

4. Simulation and Experimental

4.1. Simulation Analysis. First, the stability of $H\infty$ controller is attested through analyzing the singular values relationship between $S(s)$ and $W_1(s)$, as well as between $T(s)$ and $W_3(s)$. The sensitivity and complementary sensitivity function and the corresponding weighted function singular value relations

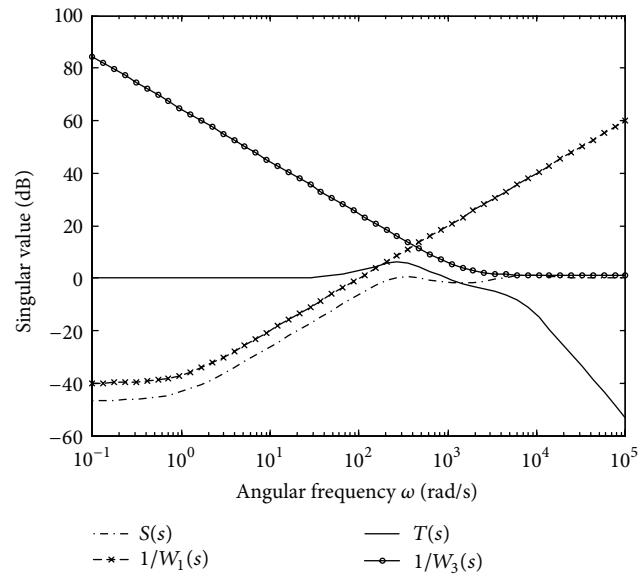

Figure 5: Sensitivity, complementary sensitivity, and the corresponding weighted function singular value relations.

are shown in Figure 5. The curves in Figure 5 are created in the "M" file of MATLAB through some command functions, the transfer functions of $\mathbf{T_c}$, $\mathbf{K}_H$, and $\mathbf{G}(s)$, and so on.

The choice principle of $W_1(s)$ is guaranteeing the anti-interference and tracking ability of the flywheel system, and the smaller the singular value of $S(s)$ is, the better the system tracking ability is. The curve of $S(s)$ should be under the curve of the $1/W_1(s)$; if it does not conform to the demand, the weighted function $W_1(s)$ must be chosen again. The choice principle of $W_3(s)$ is guaranteeing the flywheel system output to recurrence the input, and the smaller the singular value of $T(s)$ is, the smaller the system impact by compound disturbance because of model uncertainty is. The curve of $T(s)$ should also be under the curve of the $1/W_3(s)$; if it does not conform to the demand, the weighted function $W_3(s)$ must be chosen again. Figure 5 shows that the curve of $S(s)$ is under the curve of $1/W_1(s)$, and the curve of $T(s)$ is under the curve of $1/W_3(s)$, which demonstrates that the selection of weighted function in types (14) and (15) can meet the design requirements, and the solved $H\infty$ controller is appropriate.

Second, the simulation parameters of AILC are selected as $f_d = 600$ Hz, $P = 0.995$, $Q = 0.75$, $Q_1 = 0.25$, $n = 0, 1, \ldots, 99$, and the definition of "n" indicates that the AILC algorithm has 100 memory points in one control period. Figure 6 shows the rotor simulation orbits and radial run-out displacements with AILC compensation.

The flywheel has a regular circular trajectory in Figure 6(a) and a sine radial run-out displacement in Figure 6(b) without adding AILC compensation. When the AILC algorithm starts to work at 0.05 s, the circular trajectory is gradual convergence to a point and the amplitude of the radial run-out displacement is obvious attenuation. The curves change simulation result in Figure 6 testifies the AILC algorithm having good displacement compensation effect

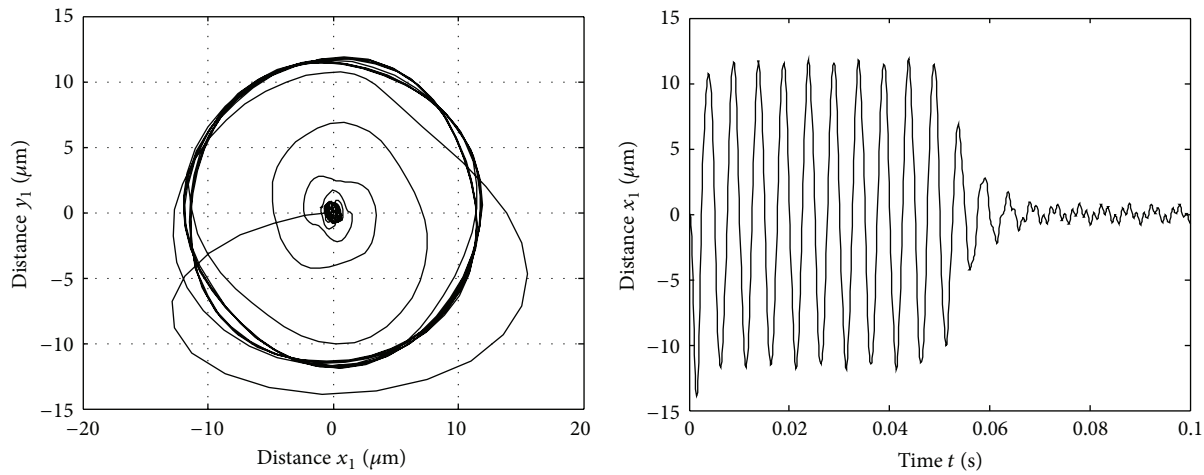

(a) Rotor position orbit

(b) Rotor run-out in axis x_1

Figure 6: Flywheel trajectory with AILC compensation.

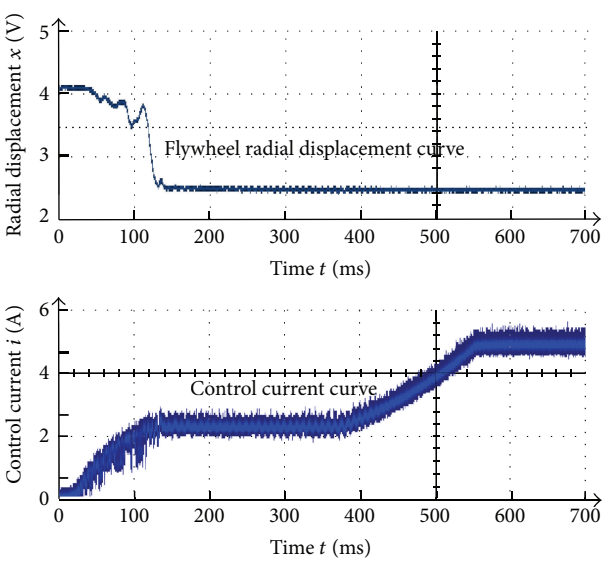

Figure 7: Flywheel displacement and control current in start-up process by $H\infty$ control.

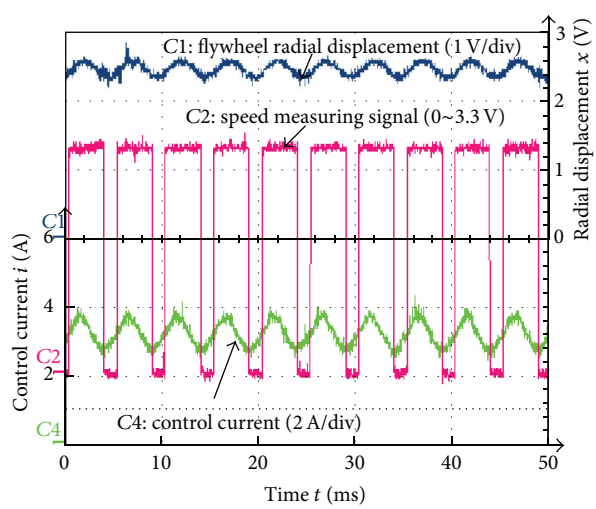

Figure 8: Flywheel displacement and control current in rotating process by $H\infty$ control and the speed measuring pulse at 600 Hz.

and ensuring the flywheel to rotate around its collection center.

4.2. Experimental Results. In Figure 7, the radial displacement voltage curve and the control current curve of the flywheel are shown in start-up process by the solved $H\infty$ controller control; the displacement voltage quickly drops to the equilibrium position (2.5 V) from the sensor calibration position (4 V). It illustrates that the $H\infty$ controller has good robust stability and can be used in the control system of vehicle maglev flywheel.

Figure 8 includes the radial displacement curve, the control current curve, and the speed measuring pulse when flywheel normal is rotating by $H\infty$ control and flywheel rotational frequency is 600 Hz. The displacement curve is a sine wave, and it can show the flywheel has mass unbalance. To restrict flywheel radial run-out, the control current also is sine having basic consistent phase with the displacement voltage. The speed measuring pulse has a voltage range from 0 V to 3.3 V; the purpose is to guarantee the pulse be captured by DSP acquisition circuit.

The compensated effect by AILC algorithm at 600 Hz is shown in Figure 9, including the radial displacement curve and the control current curve after compensation. Compared with the radial sine displacement in Figure 8, the radial displacement is balance in the position of 2.5 V, which indicates the flywheel is limited rotating around its geometric center. To limit the radial run-out and increase the active control effect, the control current amplitude is significantly larger than without compensation.

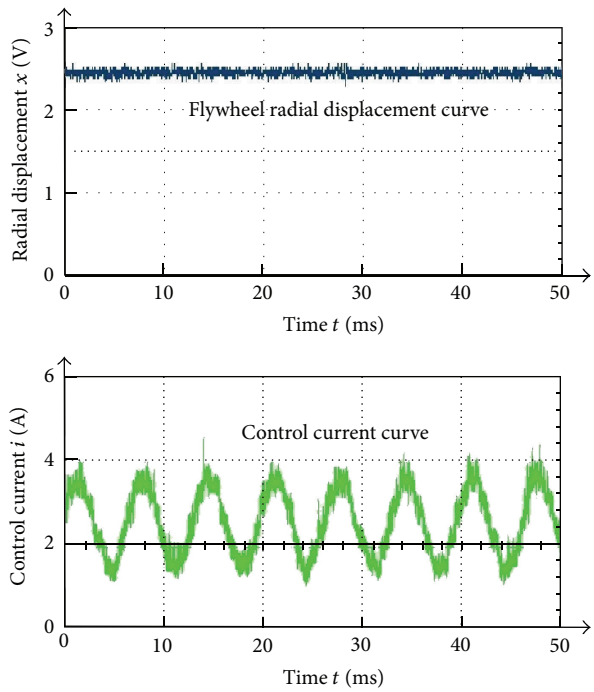

Figure 9: Flywheel displacement and control current in AILC compensation process at 600 Hz.

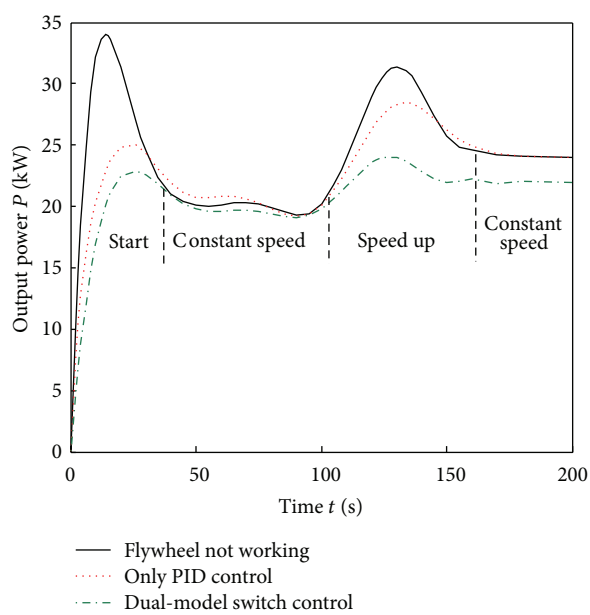

Figure 10: EV primary battery output power in different modes.

Figure 10 gives the output power curves of EV primary battery in three different modes. If flywheel is not working, the output power is about 35 kW when EV starts up; if the flywheel battery is working and only PID controlling, the output power of the primary battery is about 25 kW in EV start-up process; if the dual-model switch control strategy is acting on the flywheel, the output power reduces to 23 kW. The power change shows the flywheel has better auxiliary effect to EV primary battery when it is controlled by the dual-model switch control strategy. Similarly, the output power of EV primary battery is the smallest in the acceleration process when the dual-model switch control strategy controls the flywheel. Moreover, because the flywheel rotate speed is higher when the dual-model switch control strategy is working, EV needs lower motive power when restarting. Therefore, when maglev flywheel participates in discharge and is controlled by dual-model switch control strategy, EV primary battery output power is obviously decreased in the whole driving process, the influence on chemical characteristics of primary battery is reduced because the instantaneous discharge depth is small, and the service life of EV primary battery can be improved.

5. Conclusion

Through analyzing the nonlinear dynamic characteristics and the application on EV, one kind of dual-model control strategy based on $H\infty$ control and AILC algorithms has been studied in this paper, and the state space equation of maglev flywheel was analyzed. To improve the robust stability of flywheel control system and reduce the real-time interference, one $H\infty$ controller based on the state space equation was solved. To reduce maglev flywheel radial run-out, one adaptive iterative learning control theory was deduced, and unbalance displacement compensation was implemented. The experimental result shows the dual-model control strategy has better interference capability in maglev flywheel start-up process and has stronger active control ability relative to only PID control. The maglev flywheel based on the dual-model control can help the EV primary battery, improve its discharge characteristics, help to prolong its service life, and accelerate the development scale of electric vehicles.

Conflict of Interests

The authors declare that they have no conflict of interests regarding this paper.

Acknowledgments

This work is supported by the National Natural Science Foundation of China (51405244), the China Postdoctoral Science Foundation (2014M551634), and the Jiangsu Province Natural Science Foundation of China (BK20140880). The authors would like to thank the editor and the reviewers for their constructive comments and suggestions to improve the quality of the paper.

References

[1] E. Sortomme, *Optimal aggregator bidding strategies for vehicle-to-grid [Ph.D. thesis of Philosophy]*, University of Washington, 2011.

[2] H.-F. Dai, Z.-C. Sun, and X.-Z. Wei, "Technologies to relief un-uniformity of power batteries used in electrical vehicles," *Journal of Automotive Safety and Energy*, vol. 2, no. 1, pp. 62–67, 2011.

[3] B. Bolund, H. Bernhoff, and M. Leijon, "Flywheel energy and power storage systems," *Renewable and Sustainable Energy Reviews*, vol. 11, no. 2, pp. 235–258, 2007.

[4] M. Jiang, J. Salmon, and A. M. Knight, "Design of a permanent magnet synchronous machine for a flywheel energy storage system within a hybrid electric vehicle," in *Proceedings of the IEEE International Electric Machines and Drives Conference (IEMDC '09)*, pp. 1736–1742, May 2009.

[5] J. Abrahamsson, J. de Santiago, and J. G. Oliveira, "Prototype of electric driveline with magnetically levitated double wound motor," in *Proceedings of the 19th International Conference on Electrical Machines (ICEM '10)*, pp. 1–5, September 2010.

[6] M. S. Raymond, M. E. F. Kasarda, and P. E. Allaire, "Windage power loss modeling of a smooth rotor supported by homopolar active magnetic bearings," *Journal of Tribology*, vol. 130, no. 2, pp. 1–8, 2008.

[7] Y.-L. Xu and J.-C. Fang, "Development of low power loss energy storage flywheel," *Transactions of China Electrotechnical Society*, vol. 23, no. 12, pp. 11–16, 2008.

[8] T. A. Aanstoos, J. P. Kajs, W. G. Brinkman et al., "High voltage stator for a flywheel energy storage system," *IEEE Transactions on Magnetics*, vol. 37, no. 1, pp. 242–247, 2001.

[9] H. Qing-kai, *Nonlinear Vibration Analysis and Diagnosis Method for Fault Rotor System* , Science Press, Beijing, China, 2010.

[10] H. Gao, L. Xu, and Y. Zhu, "Unbalance vibratory displacement compensation for active magnetic bearings," *Chinese Journal of Mechanical Engineering*, vol. 26, no. 1, pp. 95–103, 2013.

[11] Z. Gosiewski and A. Mystkowski, "Robust control of active magnetic suspension: analytical and experimental results," *Mechanical Systems and Signal Processing*, vol. 22, no. 6, pp. 1297–1303, 2008.

[12] J.-M. Kim, C.-K. Kim, M.-K. Park, and K.-H. Kim, "A robust control of a magnetic suspension system with a flexible rail," in *Proceedings of the IEEE International Symposium on Industrial Electronics (ISIE '01)*, vol. 2, pp. 1309–1312, Pusan, Republic of Korea, June 2001.

[13] H. G. Chiacchiarini and P. S. Mandolesi, "Unbalanced compensation for active magnetic bearings using ILC," in *Proceedings of the IEEE International Conference on Control Applications*, pp. 58–63, Mexico City, Mexico, September 2001.

[14] C. Bi, D. Wu, Q. Jiang, and Z. Liu, "Automatic learning control for unbalance compensation in active magnetic bearings," *IEEE Transactions on Magnetics*, vol. 41, no. 7, pp. 2270–2280, 2005.